






An ever-present *Gaia* snail shell triggered by a dark matter wake

Robert J. J. Grand ^{1,2,3}★, Rüdiger Pakmor ⁴, Francesca Fragkoudi,⁵ Facundo A. Gómez,^{6,7} Wilma Trick,⁴ Christine M. Simpson ⁸, Freeke van de Voort ⁹ and Rebekka Bieri ^{4,10}

¹*Astrophysics Research Institute, Liverpool John Moores University, 146 Brownlow Hill, Liverpool L3 5RF, UK*

²*Instituto de Astrofísica de Canarias, Calle Vía Láctea s/n, E-38205 La Laguna, Tenerife, Spain*

³*Departamento de Astrofísica, Universidad de La Laguna, Av. del Astrofísico Francisco Sánchez s/n, E-38206 La Laguna, Tenerife, Spain*

⁴*Max-Planck-Institut für Astrophysik, Karl-Schwarzschild-Straße 1, D-85748 Garching, Germany*

⁵*Institute for Computational Cosmology, Department of Physics, Durham University, South Road, Durham DH1 3LE, UK*

⁶*Instituto de Investigación Multidisciplinar en Ciencia y Tecnología, Universidad de La Serena, Raúl Bitrán 1305, La Serena, Chile*

⁷*Departamento de Astronomía, Universidad de La Serena, Av. Juan Cisternas 1200 Norte, La Serena, Chile*

⁸*Argonne Leadership Computing Facility, Argonne National Laboratory, Lemont, IL 60439, USA*

⁹*Cardiff Hub for Astrophysics Research and Technology, School of Physics and Astronomy, Cardiff University, Queen's Buildings, Cardiff CF24 3AA, UK*

¹⁰*Center for Space and Habitability, University of Bern, Gesellschaftsstrasse 6 (G6), CH-3012 Bern, Switzerland*

Accepted 2023 June 27. Received 2023 June 23; in original form 2022 November 15

ABSTRACT

We utilize a novel numerical technique to model star formation in cosmological simulations of galaxy formation – called SUPERSTARS – to simulate a Milky Way-like galaxy with $\gtrsim 10^8$ star particles to study the formation and evolution of out-of-equilibrium stellar disc structures in a full cosmological setting. In the plane defined by the coordinate and velocity perpendicular to the mid-plane [vertical phase space, (Z, V_Z)], stars in solar-like volumes at late times exhibit clear spirals qualitatively similar in shape and amplitude to the *Gaia* ‘snail shell’ phase spiral. We show that the phase spiral forms at a lookback time of ~ 6 Gyr during the pericentric passage of an $\sim 10^{10} M_\odot$ satellite on a polar orbit. This satellite stimulates the formation of a resonant wake in the dark matter halo while losing mass at a rate of ~ 0.5 – 1 dex per orbit loop. The peak magnitude of the wake-induced gravitational torque at the solar radius is ~ 8 times that from the satellite, and triggers the formation of a disc warp that wraps up into a vertical phase spiral over time. As the wake decays, the phase spiral propagates several gigayears to present day and can be described as ‘ever-present’ once stable disc evolution is established. These results suggest an alternative scenario to explain the *Gaia* phase spiral, which does not rely on a perturbation from bar buckling or a recent direct hit from a satellite.

Key words: methods: numerical – Galaxy: disc – Galaxy: evolution – Galaxy: kinematics and dynamics – Galaxy: structure – galaxies: spiral.

1 INTRODUCTION

Recent large Galactic surveys such as *Gaia* (Gaia Collaboration 2018a) have now crystallized the idea that the Milky Way is in a state of dynamical disequilibrium. The Galactic disc(s) in particular harbours a great deal of structure indicative of this, including vertical asymmetries such as the warp and Monoceros Ring (e.g. Gómez et al. 2012; Slater et al. 2014; Xu et al. 2015; Poggio et al. 2018; Schönrich & Dehnen 2018) and planar stellar moving groups (see e.g. Antoja et al. 2018; Gaia Collaboration 2018b; Kawata et al. 2018; Fragkoudi et al. 2019). These features are thought to originate from rich dynamical phenomena ranging from external perturbations (e.g. Widrow et al. 2012; Xu et al. 2015; Gómez et al. 2017; Antoja et al. 2018; Laporte, Koposov & Belokurov 2022) to internal processes from bars and spiral arms (e.g. Monari et al. 2016; Fragkoudi et al. 2019; Trick, Coronado & Rix 2019; Trick et al. 2021). The detailed information now available from large Galactic surveys provide a unique opportunity to learn about these gravitational processes that

have shaped the distribution of stars in our Galaxy. Given that gravity permeates the dark sector as well as the baryonic, it is also a window into the distribution of dark matter, and perhaps even its nature.

One of the most striking and recently discovered dynamical features discovered in the Galactic disc is the so-called *Gaia* ‘phase spiral’ or ‘snail shell’ (Antoja et al. 2018; Tian et al. 2018; Laporte et al. 2019; Frankel et al. 2023): a spiral pattern in the vertical phase plane (Z, V_Z) associated with oscillations perpendicular to the Galactic plane of nearby disc stars. This feature can be seen in both the density and planar velocity (either V_ϕ or V_R) of stars in this plane, and is indicative of the phase mixing of a group of stars initially clumped together in the phase plane. The spiral shape occurs because the vertical period of oscillation is an increasing function of amplitude (anharmonic motion); therefore, stars with larger oscillations in the initial clump would take longer to traverse a phase space ellipse compared to those with smaller oscillations (see Binney & Schönrich 2018, for a thorough explanation).

There has already been a surge in activity to try to understand the origin of the initial clump of stars. Several studies have linked the phase spiral to a perturbation from a dwarf satellite (e.g. Antoja et al. 2018; Binney & Schönrich 2018). Such a perturbation can

* E-mail: r.j.grand@ljmu.ac.uk

qualitatively reproduce the phase spiral as seen in V_ϕ or V_R by generating correlated, coherent in-plane and vertical oscillations of stars entering the solar neighbourhood from both the inner and outer disc; a clump of low- V_ϕ , short vertical period inner disc stars shears into tighter spirals relative to a clump of high- V_ϕ , long vertical period outer disc stars. An obvious candidate for the perturbing satellite is the Sagittarius dwarf galaxy (hereafter Sgr), which is thought to have undergone several close pericentric passages (Purcell et al. 2011; Ruiz-Lara et al. 2020) and induced gravitational perturbations on the disc (Gómez et al. 2013). Indeed, several idealized N -body simulations have shown that earlier passages of a more massive Sagittarius are able to qualitatively reproduce the phase spiral (Laporte et al. 2019; Bland-Hawthorn & Tepper-García 2021; Hunt et al. 2021).

However, the explanation of the Sgr as the source of perturbation is not completely accepted. For example, Bennett, Bovy & Hunt (2022) conclude that the inferred present-day mass of the Sgr core remnant ($\sim 3 \times 10^8 M_\odot$; Vasiliev & Belokurov 2020) is too low to have produced the observed amplitude of the spiral on its own, although their experiments did not allow for significant mass-loss over multiple passages of Sgr (see Bland-Hawthorn & Tepper-García 2021). Nevertheless, alternative sources of perturbation such as spiral arms and/or a bar have gained traction in the literature: Khoperskov et al. (2019) advocate for a strong vertical perturbation caused by a buckling bar, Tremaine, Frankel & Bovy (2023) discuss Gaussian noise from dark matter subhaloes and giant molecular clouds, whereas Darling & Widrow (2019) discuss bending waves generated by an ad hoc vertical perturbation. It is worth noting that vertical perturbations developed by internal mechanisms typically show smaller amplitudes than those associated with external agents, such as a large satellite (e.g. Faure, Siebert & Famaey 2014; Monari et al. 2016; Gómez et al. 2021). The recent work of García-Conde et al. (2022) found from their cosmological simulation that several relatively light satellites appear to be connected with the genesis of a phase spiral-like features, which indicates that the situation is not fully understood and could be more complex than previously imagined.

Another class of perturbation arise from collective effects from resonant wakes generated in the dark matter halo by a passing satellite (e.g. Weinberg 1995, 1998; Vesperini & Weinberg 2000). Cosmological simulations have shown that these wakes can induce dynamical perturbations more than an order of magnitude larger than those from the satellite itself, and form galaxy-wide disc warps and corrugation patterns with features similar to that of the Milky Way’s Monoceros Ring (Gómez et al. 2016, 2021). Using tailored N -body simulations of the impact of an Sgr-like galaxy on an equilibrium stellar disc, Laporte et al. (2018, 2019) showed that the early pericentric passages of Sgr stimulate the growth of a dark matter wake and the appearance of phase spirals. However, at late times, the wake impact becomes negligible compared to the direct impact of Sgr. The latter ‘resets’ the vertical disc structure into a phase spiral configuration likened to the *Gaia* snail shell. Thus, the nature of the perturbation from which the observed feature arises is attributed directly to Sgr itself.

Nearly all of the theoretical work discussed above that explicitly studies the phase spiral adopts either toy or idealized N -body models (to the author’s knowledge, the single exception is García-Conde et al. 2022). These models do not include cosmologically grown stellar discs (and therefore have no memory of stellar populations formed during past epochs) that could respond differently to perturbations relative to smooth equilibrium discs. Nor do they include the array of perturbations inherent to a cosmological setting, such as misaligned gas discs, the spectrum of subhaloes and satellites expected for the Lambda cold dark matter (Λ CDM) paradigm, and a non-spherical

dark matter halo. Cosmological zoom-in simulations model all of these processes, but their limited resolution typically precludes the study of delicate and detailed dynamical features like the phase spiral. For example, Gómez et al. (2016) globally characterized the vertical response of a galactic disc simulated on a fully cosmological context, but lacked the resolution to study its response in local solar-like volumes. For cosmological simulations to match the detail provided by $\sim 10^8$ star particles now attained by idealized models (Bland-Hawthorn & Tepper-García 2021; Hunt et al. 2021), tens of millions of CPU hours per simulation are required.¹ This substantial computational expense, which is mainly incurred by the hydrodynamic calculation involving large numbers of gas particles/cells, hinders the production of cosmological simulations capable of resolving detailed dynamical structures such as the snail shell.

In this paper, we employ a new technique for star formation in cosmological simulations – called SUPERSTARS, which significantly boosts the stellar resolution to $\gtrsim 10^8$ star particles without the need to increase the gas resolution. This approach yields significant advantages: it provides access to new dynamical scales for stars at a substantially reduced computational cost, and side-steps the most significant challenges to numerical convergence, which are driven almost entirely by changes to gas resolution. We describe this technique in Section 2. In Section 3, we study the nature and origin of dynamical features analogous to the *Gaia* ‘snail shell’. We show that the simulated disc develops a spiral structure in vertical phase space during the epoch of disc formation, and tie its origin to a dark matter halo wake. We show that this feature lasts until the present day, by which time it has decayed to an amplitude and shape quantitatively similar to the *Gaia* phase spiral. In Section 4, we summarize our conclusions and discuss our findings in the context of earlier work.

2 SIMULATIONS

2.1 The AURIGA model

The simulated galaxy presented in this paper is a re-simulation of one of the Milky Way-mass systems from the AURIGA project (Grand et al. 2017, 2018), specifically the halo presented in Grand et al. (2021) (referred to as Au 6 in AURIGA nomenclature). This halo has a mass of $M_{200} = 1.03 \times 10^{12} M_\odot$ at redshift zero, where M_{200} is defined as the mass contained inside the radius at which the mean enclosed mass density equals 200 times the critical density of the Universe. The parent dark matter-only cosmological simulation has a comoving periodic box size 100 Mpc, and adopts the following parameters for the standard Λ CDM cosmology: $\Omega_m = 0.307$, $\Omega_b = 0.048$, $\Omega_\Lambda = 0.693$, and a Hubble constant of $H_0 = 100h \text{ km s}^{-1} \text{ Mpc}^{-1}$, where $h = 0.6777$, taken from Planck Collaboration XVI (2014). At redshift 127 (the starting redshift), the resolution of the dark matter particles of the Lagrangian region from which this halo forms is increased and gas is added to create the initial conditions of the zoom simulation. At redshift zero, this high-resolution region has a radius of the order of ~ 1 Mpc.

The simulation was performed with the magnetohydrodynamical code AREPO (Springel 2010; Pakmor et al. 2016), and the AURIGA galaxy formation model, which includes the following: primordial and metal line cooling; a uniform ultraviolet background that gradually increases to completion at $z = 6$; a model for star formation

¹Few cosmological simulations have attained such a high stellar particle resolution, namely the Justice League Mint Condition simulation (Applebaum et al. 2021) and a simulation from the AURIGA project (Grand et al. 2021).

that activates for gas densities larger than $0.1 \text{ atoms cm}^{-3}$ (Springel & Hernquist 2003); magnetic fields (Pakmor, Marinacci & Springel 2014; Pakmor et al. 2017, 2018); gas accretion on to black holes; and energetic feedback from active galactic nucleus and Type II supernovae (SNII; see Vogelsberger et al. 2013; Marinacci, Pakmor & Springel 2014; Grand et al. 2017, for more details). Each star particle is treated as a single stellar population of given mass, age, and metallicity. Stellar mass-loss and metal enrichment from Type Ia supernovae and asymptotic giant branch stars are modelled according to a delay time distribution, and metals from SNII are injected promptly. The AURIGA model has been shown to produce realistic spiral disc galaxies that are broadly consistent with a number of observations including star formation histories, stellar masses, sizes, and rotation curves of Milky Way-mass galaxies (Grand et al. 2017), the distribution of H I gas (Marinacci et al. 2017), the stellar halo properties of local galaxies (Monachesi et al. 2019), stellar disc warps (Gómez et al. 2017), the properties and abundance of galactic bars (Fragkoudi et al. 2020, 2021) and bulges (Gargiulo et al. 2019), the properties of magnetic fields in nearby disc galaxies (Pakmor et al. 2017, 2018), and the luminosity function of satellite galaxies (Simpson et al. 2018).

In the study of Grand et al. (2021), we presented the hitherto highest resolution cosmological hydrodynamic zoom simulation of a Milky Way-mass halo; the baryonic and dark matter mass resolutions of the simulation are $\sim 800 M_\odot$ and $6 \times 10^3 M_\odot$, respectively. In the AURIGA nomenclature, this resolution is given the shorthand ‘level 2’. Apart from the significant computational expense (~ 15 million CPU h), this study highlighted two significant issues: (i) an ~ 30 per cent systematic increase in stellar mass of the main galaxy for each factor 8 increase in mass resolution (see table 2 of Grand et al. 2021); and (ii) a breakdown in the black hole centring algorithm at very high (level 2) gas resolution with negative consequences for disc formation. The former is a qualitatively generic problem for all hydrodynamic simulations, whereas the latter is a new obstacle. Both, however, are related to increases in gas resolution. This situation motivates a different approach to model stellar dynamics in cosmological simulations in which the mass resolutions of collisionless components are enhanced relative to the gas.

2.2 The SUPERSTARS method

We adopt a newly developed method called SUPERSTARS, which achieves both a very high stellar resolution and removes the issues described above, namely (i) the large computational cost and (ii) systematic changes with gas resolution. This method will be fully described in Pakmor et al. (in preparation), and the full suite of simulations will be presented in Fragkoudi et al. (in preparation). Here, we briefly summarize the essence of the method. Instead of forming a single star particle of a mass approximately equal to that of the gas cell from which it spawned, SUPERSTARS forms a group of lower mass star particles instead. The birth positions are identical for each of the star particles in one group. Their velocities are set to the velocity of the parent gas cell plus a random isotropic component. The size of the isotropic component is drawn randomly from a Gaussian distribution with a width set by the minimum of the local sound speed and velocity dispersion of its neighbouring gas cells. We ensure that the total contributions of all random components of one group cancel to conserve total momentum in the simulation. The chemical evolution is handled in exactly the same manner as the original AURIGA simulations. The number of star particles formed per group is in principle arbitrary, but is naturally limited by the available

computational resources. In the simulation discussed in this paper, we retain the level 4 gas resolution ($\sim 5 \times 10^4 M_\odot$) and form 64 star particles per group and star-forming gas cell. This achieves the same stellar mass resolution ($\sim 800 M_\odot$) as the simulation presented in Grand et al. (2021) with the highly desirable benefits of much improved numerical convergence (including a well-behaved black hole centring algorithm) and a more than 10 times reduction in the overall computational cost. As will be shown in Pakmor et al. (in preparation), the larger dark matter to stellar particle mass ratio that this technique entails does not enhance artificial scattering of particles found for lower resolution large cosmological volume simulations (Ludlow et al. 2019, 2021).

In the context of this study, SUPERSTARS resolves detailed Galactic structure of the kind recently observed by large surveys such as *Gaia* in the presence of an array of complex dynamical phenomena inherent to galaxy formation. This is complementary to studies based on toy models and idealized N -body simulations that make up the vast majority of the current literature on the subject.

3 RESULTS

3.1 Present-day phase spiral properties

In this section, we present the properties of the disc and vertical phase spiral at redshift zero, with reference to the *Gaia* snail shell where appropriate.² The top row of Fig. 1 shows a face-on view of the present-day stellar disc colour-coded according to various properties: the azimuthal stellar overdensity in the disc plane (left-hand panel); the mean radial velocity (second panel); the mean vertical velocity (third panel); and the mean vertical height (fourth panel). Here, we note the presence of a weak bar and clear spiral structure stretching from the ends of the bar into the outer disc. In a similar morphological pattern, the mean radial velocity betrays streaming motions of magnitude $\sim 10 \text{ km s}^{-1}$ correlated with the bar/spiral overdensities. A mild corrugation pattern is evident in the third and fourth panels of the top row of Fig. 1 as oscillations in Z and V_z along radial ‘spokes’ of constant azimuth; the pattern appears to span from the solar circle to the edge of the galaxy.

The second and third rows of Fig. 1 show the overdensity of the V_z - Z distribution of star particles within 3 kpc of eight solar-like positions (spread equidistant in azimuth along a cylindrical radius of 8 kpc in the disc mid-plane), where each coordinate is normalized such that they are dimensionless (as done in Hunt et al. 2021, for example). For the normalization factors, we calculate, for each snapshot, the standard deviation of the vertical position³ and velocity (h_z and σ_z , respectively) of star particles younger than 3 Gyr in a solar annulus of width and height equal to 2 kpc. This selection ensures that we calculate a reasonable normalization for disc stars at solar-like positions. At the present day, the values are $h_z = 530 \text{ pc}$ and $\sigma_z = 23 \text{ km s}^{-1}$, respectively. To calculate the overdensity value of each pixel in this surface of section, we first smooth the raw distribution with a 2D Gaussian kernel of width equal to 0.5 for both coordinates to yield

²We note that the purpose of this section is not to make detailed quantitative comparisons with observations, but rather place our results in the context of the literature.

³Note that this is not the same as the scale height, Z_0 , of a fitted density profile typically used to measure the thickness of discs, such as the $\text{sech}^2(Z/Z_0)$ profile. For this simulated galaxy, the thin and thick disc scale heights are $Z_{0,\text{thin}} = 363 \text{ pc}$ and $Z_{0,\text{thick}} = 1107 \text{ pc}$, respectively. These values are consistent with current estimates for the Milky Way’s thin and thick discs (see Bland-Hawthorn & Gerhard 2016, and references therein).

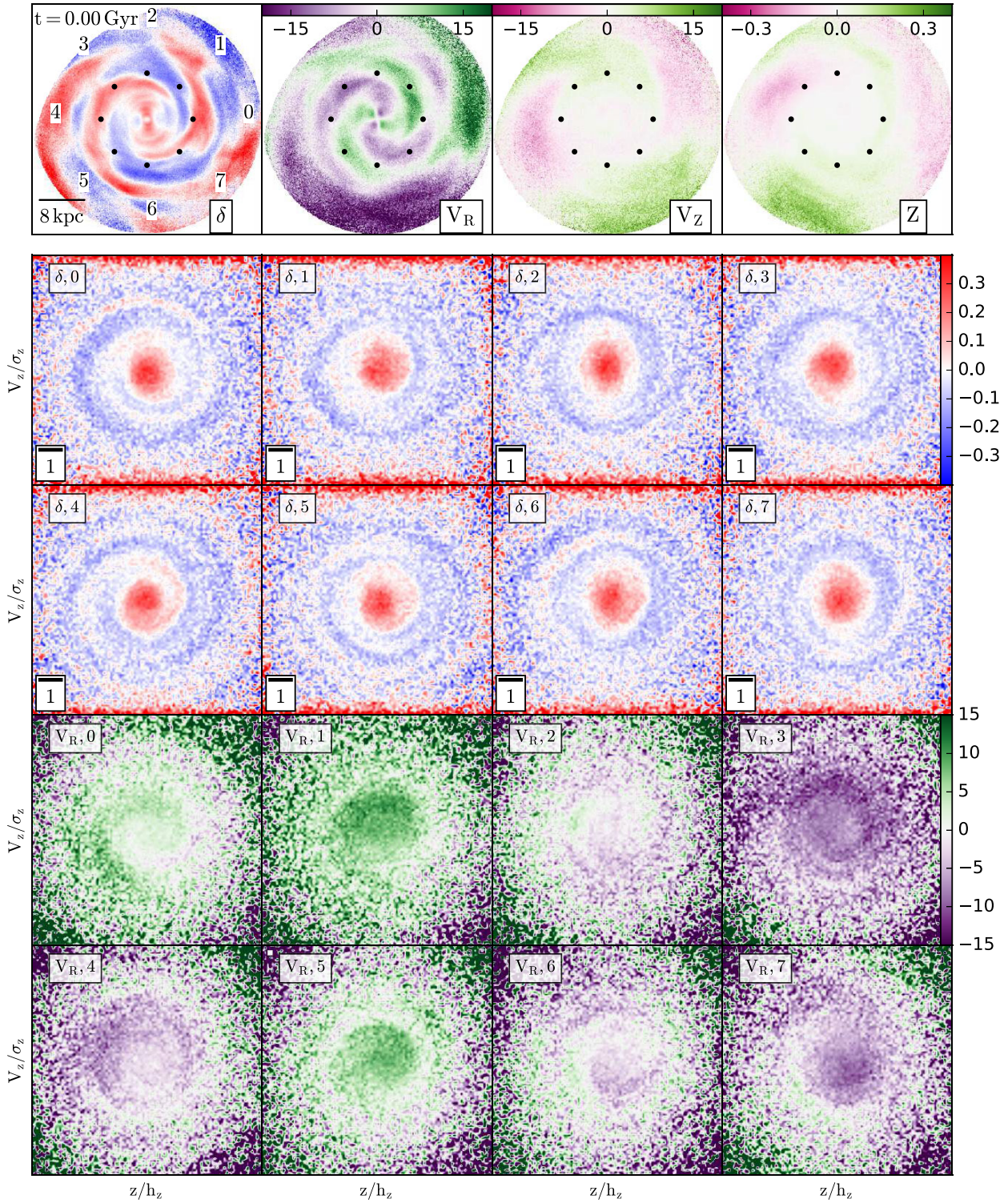


Figure 1. *Top row:* 40 kpc \times 40 kpc face-on projections of various quantities for star particles within 1 kpc height above/below the mid-plane at redshift zero: the azimuthal overdensity (leftmost panel); the mean radial velocity (km s^{-1} , second panel); the mean vertical velocity (km s^{-1} , third panel); and the mean vertical height (kpc, fourth panel). Black symbols mark the positions of eight solar-like positions placed equidistant along a ring of 8 kpc radius. *Second and third rows:* the overdensity of star particles located within 3 kpc of each solar-like position in the dimensionless vertical phase plane (see text for details). *Fourth and fifth rows:* as above, but coloured according to radial velocity (km s^{-1}). The phase space spiral is visible at all eight solar-like locations. A high-cadence (5 Myr time resolution) animation of this figure in the co-rotating frame (at $R = 8 \text{ kpc}$) can be viewed at https://www.mpa.mpg.de/auriga/movies/multi_halo.6.sf64.mp4. Fig. A1 in Appendix A is the equivalent figure for a ‘level 4’ simulation, which demonstrates that phase spirals are not resolved at that resolution.

a mean density map. We then divide the original unsmoothed map by the mean density map and subtract 1 from each pixel, such that pixels with a positive (negative) value are over(under)densities. Phase spiral structures are present at each solar-like location and exhibit a variation in the detailed morphological appearance and amplitude: at some solar-like positions (e.g. position 0), we see clear phase spirals⁴ with amplitudes of roughly 0.1 where they are clearly visible (typically at dimensionless vertical phase space radii of 0.5–2.5). We note that phase spiral features are not resolved for the ‘level 4’ resolution of this simulation (see Fig. A1). The dimensionless phase spiral amplitudes shown in Fig. 1 are similar to the amplitudes of the dimensional phase spiral (without normalizing Z and V_z by h_z and σ_z , respectively), which is demonstrated in Fig. A2. These amplitudes are within ~ 0.05 of what is reported for the *Gaia* snail shell by Laporte et al. (2019) from *Gaia* Data Release 2 (DR2) and by Antoja et al. (2023) and Hunt et al. (2022) for *Gaia* DR3. However, just as in idealized models (e.g. Laporte et al. 2019; Bennett et al. 2022; Hunt et al. 2022), the dimensional phase spiral in this cosmological simulation extends farther than the *Gaia* snail shell (see Appendix A and Fig. A2).

The fourth and fifth rows of Fig. 1 are similar to the second and third rows but show the mean galactocentric radial velocity of star particles in each pixel. First, we note that the average radial velocity in each vertical phase space varies across the disc; the baseline of the radial velocity fluctuations in regions in which the mean radial streaming velocity is outward (particularly positions 1 and 5; see second panel of the top row) is shifted such that the minimum velocity is only just below 0, and vice versa for positions 3 and 4. Note that the mean radial velocity in each solar-like position oscillates between inward and outward as the azimuth changes, which appears correlated to spiral arm overdensities. Taking into account this variation among different solar-like positions, we deduce the radial velocity amplitude of the phase spiral to be approximately 10 km s^{-1} , which is comparable to that of the observed phase spiral (e.g. Laporte et al. 2019).

Several observational studies have dissected the vertical phase spiral as a function of age. One of the first such studies is Tian et al. (2018), who analysed data from the Large Sky Area Multi-Object Fibre Spectroscopic Telescope (LAMOST) and *Gaia* DR2 and showed that the phase spiral is present among groups of coeval stellar populations younger than 6 Gyr, except perhaps for the very youngest stars (that formed less than 500 Myr ago), which may not exhibit a clear spiral. However, the subsequent studies of Laporte et al. (2019) and Bland-Hawthorn et al. (2019) used isochrone ages derived by Sanders & Das (2018) and age estimates from the GALactic Archaeology with HERMES (GALAH) survey, respectively, to show the spiral to be present for all ages. As these studies discuss, this sort of dissection may help date the putative perturbation. To explore this idea in our simulation, we show in Fig. 2 the vertical phase space overdensity for separate coeval stellar populations at two of the solar-like positions shown in Fig. 1 (positions 4 and 6; separated in azimuth by 90°). Star particles that formed between 2 and 6 Gyr ago (shown in the second and third rows of Fig. 2) show the strongest phase spirals. The oldest age group shows (at most) very faint signs of a phase spiral, likely because this population is kinematically hotter than the younger populations and therefore does not respond as coherently to dynamical perturbations

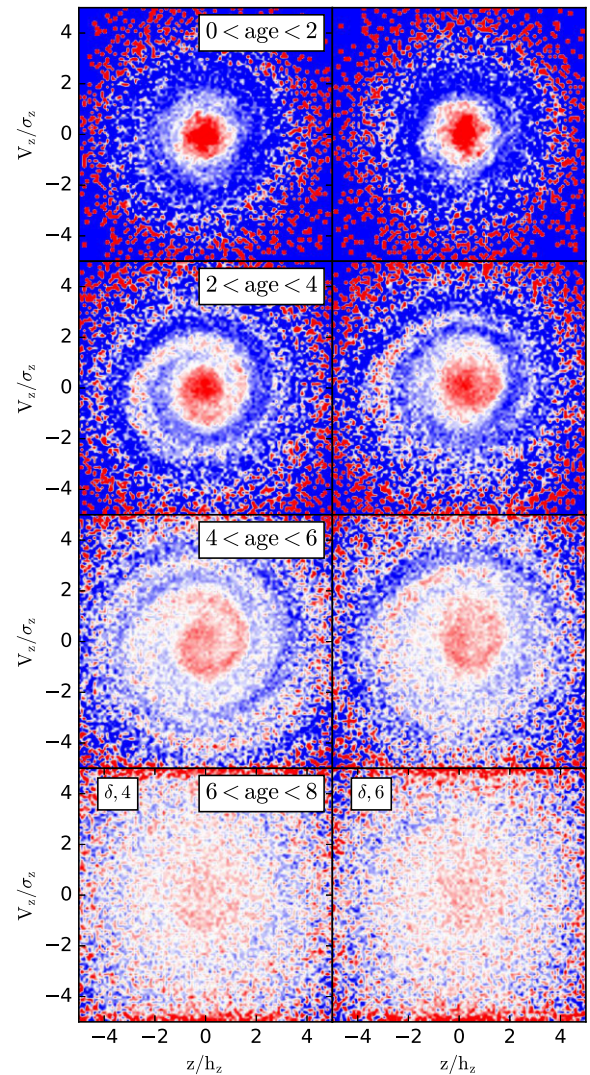


Figure 2. The vertical phase plane for star particles of different ages within 3 kpc spheres at two different solar-like positions: volumes 4 (left-hand column) and 6 (right-hand column) as indicated in Fig. 1. From top to bottom, the age groups are as follows: younger than 2 Gyr; between 2 and 4 Gyr old; between 4 and 6 Gyr old; and between 6 and 8 Gyr old. The phase spiral is clearest in the two intermediate age groups (second and third rows); however, very faint signs are visible in the oldest age group.

as the latter. This is consistent with the work of Gómez et al. (2016), who showed that satellite perturbations excited global warp and corrugation structures that were strongest in the youngest stellar populations. However, a lack of signal in stars older than 6 Gyr and younger than 2 Gyr is in contrast with the observational data presented by Laporte et al. (2019) and Bland-Hawthorn et al. (2019). We will discuss these results further in Section 4.

In Fig. 3, we show the vertical phase plane for star particles within 3 kpc spheres centred on positions along a ring of radius 14 kpc (but use the same normalization factors as for the solar-like positions in order to compare their relative shapes). The same age trends of the phase spirals described above for solar-like positions hold also for the outer disc; therefore, we show only star particles aged between 2 and 6 Gyr old in order to highlight the outer disc phase spiral properties clearly. We note two key differences compared to the spirals at solar-like positions: (i) the spirals are compressed along

⁴Note the Archimedean shape of these spirals ($r = a\theta$), as opposed to logarithmic spirals ($r = ae^{\theta \cot b}$) typically discussed in the context of galactic spiral arms (Binney & Tremaine 2008).

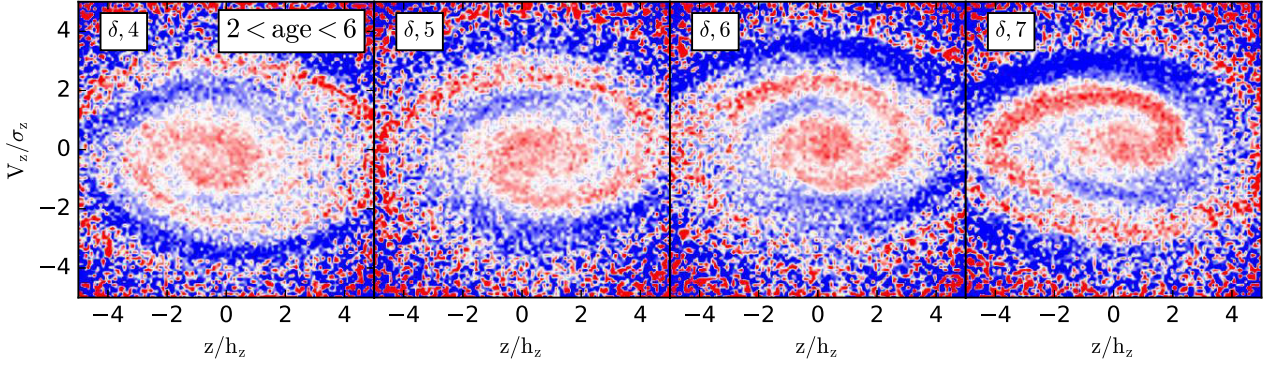


Figure 3. Similar to Fig. 2, but for star particles between 2 and 6 Gyr old within 3 kpc spheres centred on positions along a ring of radius 14 kpc.

the vertical velocity axis relative to the vertical height axis, reflecting the lower vertical restoring force of the lower surface density outer disc; and (ii) the spirals are more loosely wound (fewer wraps) owing to the lower vertical frequencies and hence longer dynamical time-scales of stars in the outer disc. These trends are consistent with those found in *Gaia* DR2 data and other simulations (see e.g. Laporte et al. 2019; García-Conde et al. 2022). Note also that these positions (4–7) span 135° in azimuth (see the top-left panel of Fig. 1) and cover a downward and upward moving section of the corrugation pattern (see the third and fourth panels of the top row of Fig. 1). This translates to spirals in the Z – V_z plane that move through approximately 180° from position 4 to position 7, and provides a flavour of the kind of variation that could be present in future observations covering broader swathes of the disc.

3.2 The evolution of the phase spiral

Having shown that the morphology and strength of our simulated present-day phase spiral are similar to the Milky Way’s snail shell, we now focus on its formation and evolution. The top two rows of Fig. 4 show an ~ 3 Gyr time sequence of the vertical height and velocity maps of the disc viewed face-on. The bottom row shows, for each snapshot, the vertical phase space overdensity of star particles in a 3 kpc volume centred at a solar-like location (indicated in each panel and selected to show the phase spiral particularly clearly). The first column shows this information for the snapshot $t_{\text{lookback}} = 6.5$ Gyr: the vertical height and velocity maps show a clear warp that stretches from the central disc to radii beyond the solar-like positions (again marked by the black symbols). This warp manifests as an off-centre overdensity in Z – V_z space (lower left-hand panel). We will show in Section 3.3 that this occurs immediately after the close pericentric passage of a satellite galaxy of infall mass of $\sim 10^{10} M_\odot$. Over time, the disc warp winds into a corrugation pattern, the precise morphology of which evolves according to the radial dependence of torques from the inner disc and outer halo (see Briggs 1990; Shen & Sellwood 2006; Gómez et al. 2017, for detailed explanations). In the vertical phase plane at $t = 5.58$ Gyr, the distribution becomes more wrapped and a two-armed phase spiral is seen in Z – V_z space at the solar location 4, which is in closest proximity to the disc crossing point of a satellite (we return to this in Section 4). However, this two-armed phase spiral is a local feature and lasts only approximately 100 Myr. The lower third panel (~ 50 Myr later) and lower fourth panel (a further ~ 1.3 Gyr later) show clear one-armed vertical phase

spirals: as phase mixing proceeds, the spiral becomes more tightly wound (characterized by more wraps) owing to the anharmonic motion discussed earlier. This time sequence clearly connects the phase spiral to an initially large-scale bisymmetric warp, and thus supports the global nature of its origin (see Laporte et al. 2019, for an idealized case).

To quantify the evolution of the phase spiral strength, we calculate the amplitudes of the $m = 1$ and $m = 2$ terms of a discrete Fourier transform of the particles in the vertical phase plane:

$$A = \sqrt{W_c^2 + W_s^2}, \quad (1)$$

where

$$W_c = \sum_i^N \cos m\theta_i / N; W_s = \sum_i^N \sin m\theta_i / N, \quad (2)$$

and N is the number of particles, and θ_i is the angular coordinate of the i th particle in this plane. The phase spiral appears well resolved in the dimensionless distance range of 0.5–2.5; therefore, we consider particles within this region only in order to avoid spurious measurement effects. We bin star particles into 10 equally spaced bins in dimensionless distance, calculate the amplitude in each bin, and take the median amplitude across all bins for each solar position.⁵ The evolution of the amplitudes of the $m = 1$ mode and the $m = 2$ mode are shown in Fig. 5: individual solar-like positions are represented by circles and the medians of these values for each time are shown by solid curves. The $m = 1$ mode emerges at early times as the disc grows in earnest at $t_{\text{lookback}} \sim 6$ –7 Gyr, followed by a gradual decay lasting several billion years before reaching a present-day amplitude of $\sim 0.1 \pm 0.05$. The $m = 2$ mode amplitude is much weaker at all times, and only attains $A \gtrsim 0.1$ at early times for brief periods at a subset of locations.

3.3 The nature of the perturbation

To understand the nature of the perturbation causing the phase spirals, we analyse the effects of possible perturbing sources, such as misaligned cold gas discs, dark matter, and satellites/subhaloes. As discussed earlier, the last of these has been extensively studied in the context of idealized simulations of the Sgr dwarf impact on a stellar

⁵The values obtained for the median amplitude at a given time and solar-like position do not depend heavily on bin size.

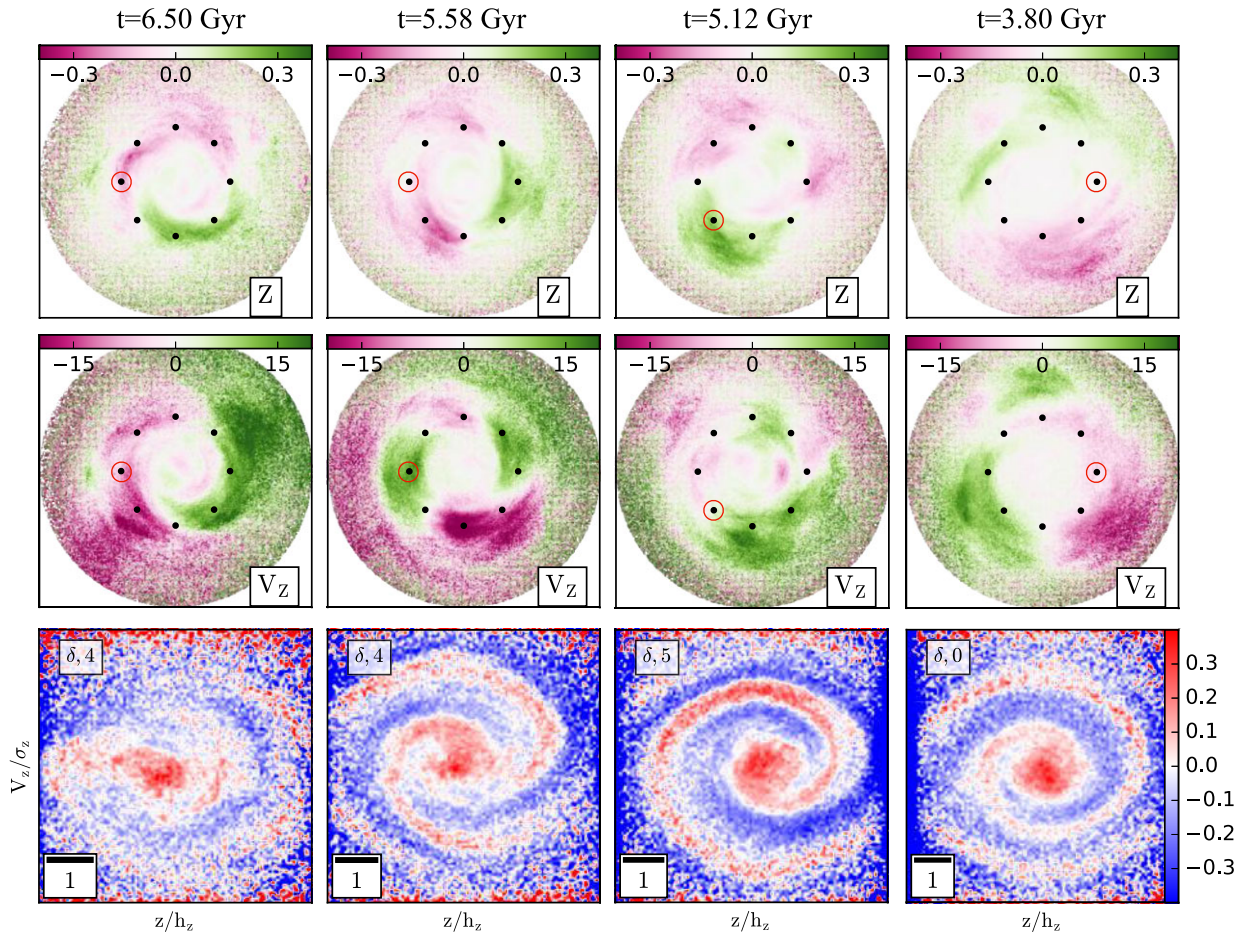


Figure 4. Time evolution of the warp/corrugation and snail shell. *First and second rows:* the mean vertical height and vertical velocity of stars for face-on apertures of $40 \text{ kpc} \times 40 \text{ kpc}$ at a series of times. Colour bars indicate the colour scale in units of kpc and km s^{-1} , respectively. Black symbols mark the locations of eight solar-like positions. *Third row:* the phase spiral overdensity at a solar-like position (indicated by the label in the top-left of each panel, and by the red circle in the first and second rows), selected to clearly show the structure at each time. The size of the phase plane is indicated by the scale bar in the lower-left corner of each panel; note that the aperture becomes larger from left to right as the normalization factors (h_z, σ_z) decrease with time owing to upside-down formation (e.g. Grand et al. 2016). These snapshots illustrate the formation of a global warp pattern (first column) that quickly starts to wind up (first two rows). As shown in the last row, a short-lived ($\sim 100 \text{ Myr}$) two-armed phase spiral emerges shortly after the onset of the warp (second column). Subsequently, a clear one-armed phase spiral develops (third column) and proceeds to wind up and decrease in strength over time (fourth column). We remind the interested reader of the animation at https://www.mpa.mpg-garching.mpg.de/auriga/movies/multi_halo_6_sf64.mp4, which shows the evolution of the phase spiral at each solar-like position.

disc. Dark matter halo torques (through, for example, dark matter wakes) have been found to have a significant impact on the stellar disc; it has been shown to be a key mechanism in the formation of galactic warps and corrugation patterns (e.g. Gómez et al. 2016, 2021; Laporte et al. 2018). In addition, prior cosmological simulations (e.g. Scannapieco et al. 2009) have shown that a misalignment between cold gas and the stellar disc can have a significant dynamical (even destructive) impact on the stellar disc. However, with the exception of the recent study of García-Conde et al. (2022), cosmological simulations have not explicitly resolved/studied ‘snail shell’-like features, and therefore their connection to the aforementioned phenomena is unclear. In this section, we study the impact of each of these perturbing sources and isolate the main driver behind the phase spiral in our simulation.

First, we focus on the orientation of cold gas with respect to the disc as it grows over time. Fig. 6 shows the evolution of the cosine of the angle between the minor axis of the stellar disc and that of two different volumes of cold star-forming gas: that contained within 15 kpc, and that found at radii between 15 and

30 kpc. At times earlier than 4 Gyr, the edge of the stellar disc⁶ is smaller than 15 kpc. Up to this time, the cold gas inside 15 kpc is never more than 5° out of alignment with the stellar disc. At $t_{\text{lookback}} = 4 \text{ Gyr}$, the stellar disc reaches a size of 15 kpc and continues to grow as it sustains near-complete alignment with the cold gas within 30 kpc for the remainder of the evolution. The near-perfect alignment between the cold gas disc and the stellar disc does not produce a significant large-scale torque; therefore, we conclude that misaligned gas is not a driver of the phase spiral in this simulation.

We now turn to the impact of satellites and dark matter. To calculate their effect, we follow the procedure of Gómez et al. (2016) that we briefly describe here for completeness. We define two rings with radii 14 and 8 kpc, and, at every simulation snapshot, select disc particles

⁶Here, we define the edge of the disc, R_1 , as the radius at which the surface mass density falls to $1 \text{ M}_\odot \text{ pc}^{-2}$; the surface density drops off rapidly for larger radii.

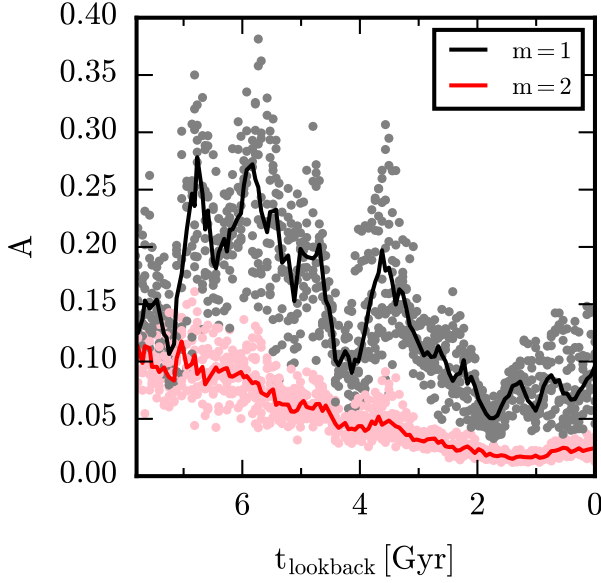


Figure 5. The amplitude of the $m = 1$ mode (black/grey) and $m = 2$ mode (red/pink) phase spiral overdensity (see Section 3.2 for details) at each of the eight solar-like positions (dots) as a function of lookback time. The medians of each mode amplitude across all positions are shown by the curves. The $m = 1$ mode peaks in amplitude at $t_{\text{lookback}} \sim 6\text{--}7$ Gyr, then proceeds to gradually decay to its present-day shape and strength depicted in Fig. 1. The $m = 2$ mode is weaker than that of the $m = 1$ mode at all times.

within two separate galactocentric shells: $13.5 < r < 14.5$ kpc and $7.5 < r < 8.5$ kpc. We diagonalize the mass tensor associated with each of these particle subsets to obtain the orientation of the rings with respect to an inertial frame. For each case, the whole system is rotated such that a given ring’s plane is aligned with the X – Y plane. We then evenly sample 1000 positions along each ring and compute the torque on the ring from dark matter particles as

$$\boldsymbol{\tau}_{\text{DM}}^{\text{shell}} = \sum_{i=1}^{1000} \mathbf{r}_i \times \mathbf{F}_i^{\text{shell}}, \quad (3)$$

where \mathbf{r}_i represents the galactocentric distance vector to the i th test particle along a ring and

$$\mathbf{F}_i^{\text{shell}} = \sum_{j=0}^{N_{\text{shell}}} \mathbf{F}_{ij} \quad (4)$$

is the gravitational force vector imparted on the i th test particle by N_{shell} dark matter particles enclosed within a given spherical shell. For our purpose of identifying the source responsible for driving the phase spiral, we shall concern ourselves with the magnitude of the torque in the directions parallel to the ring’s plane, τ_{XY} , (i.e. the X – Y component of torque that can tilt the disc plane; the Z -component of the torque only affects the magnitude of the angular momentum).

The results are shown in Fig. 7 for the test particle rings of 8 (left-hand panel) and 14 kpc (right-hand panel) radii, respectively. We focus on the time period spanning from $t_{\text{lookback}} = 8$ Gyr to the present day because this period contains most of the evolution of the (thin) disc where phase spirals are expected to develop. The total torque from dark matter particles acting on each ring is clearly most dominant during the first half of this evolutionary period, and exhibits peaks approximately 6 Gyr ago. By subdividing the contributions from different spherical shells, we see that dark matter within 20 kpc of the galactic centre dominates the torque on the solar ring, whereas

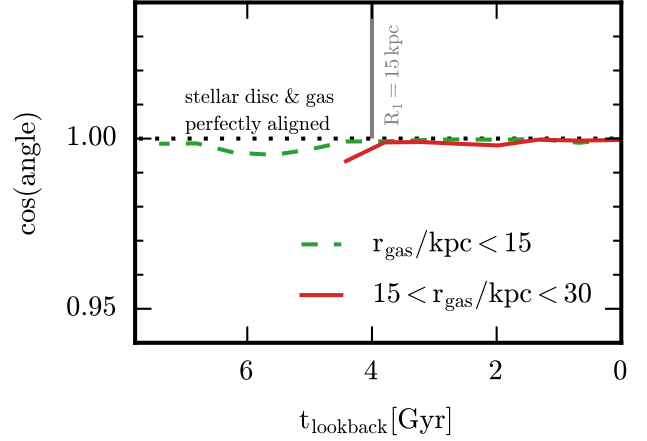


Figure 6. Evolution of the cosine of the angle between the minor axis of the stellar disc and of the cold gas in different volumes indicated in the legend. The dotted black line marks the value corresponding to perfect alignment. The time at which the disc attains a size of 15 kpc is marked by a vertical grey line; the stellar disc is smaller than 15 kpc for times earlier than 4 Gyr lookback time. Therefore, the gas within and around the disc is never more than 5° out of alignment with the stellar disc: cold gas does not impart a significant torque on the disc.

the torque on the outer disc is dominated by material between 10 and 50 kpc. After $t_{\text{lookback}} = 4$ Gyr, the torque is much diminished, although remains ever-present until the present day. In Appendix B, we verify that this torque is numerically well converged.

The circular symbols in Fig. 7 depict the torque imparted on each ring by satellite galaxies (multiplied by a factor of 4 to aid comparison to the dark matter-induced torque) and are coloured according to their total mass. Note that the spike in torque imparted by a satellite of $\sim 10^{10} M_\odot$ at around the lookback time of 6.5 Gyr precedes the peak in dark matter torque by the order of ~ 100 Myr. Fig. 8 shows the evolution of the galactocentric distance (top panel), vertical height and cylindrical radius (middle panel), and the total mass (bottom panel) of this satellite. Interestingly, the orbit and mass-loss history of this satellite up to the third or fourth pericentric passage appears qualitatively consistent with some models of Sgr (e.g. Vasiliev & Belokurov 2020; Hunt et al. 2021), albeit occurring some gigayears prior to the real Sgr. Its mass is $3 \times 10^{10} M_\odot$ prior to infall at $t_{\text{lookback}} \sim 8.5$ Gyr. The next pericentric passage occurs ~ 2 Gyr later on a near-polar orbit with a relative vertical velocity of $\sim 400 \text{ km s}^{-1}$, and corresponds to the time at which peak satellite-induced torque is attained. Incidentally, this rapid encounter correlates with the onset of the local two-armed phase spiral feature shown in the lower panel of the second column in Fig. 4: likely a manifestation of satellite-induced ‘breathing modes’⁷ (as described in e.g. Widrow et al. 2014; Hunt et al. 2022). Subsequent pericentric passages of this satellite register decreasing values of τ_{XY} , particularly on the outer disc ring, as its mass decreases owing to tidal stripping.

An important feature seen in (particularly, the right-hand panel of) Fig. 7 is that peaks in dark matter torque either coincide with (or follow shortly after) peaks of satellite-induced torque. This is a smoking-gun signature of dark matter halo wakes that form behind satellite galaxies and amplify to produce a gravitational torque on the

⁷A breathing mode manifests as a two-armed spiral in the Z – V_Z plane as the disc vertically expands and contracts symmetrically about the mid-plane, contrary to the one-armed bending mode where the disc is locally displaced as a whole into an asymmetric oscillation about the mid-plane.

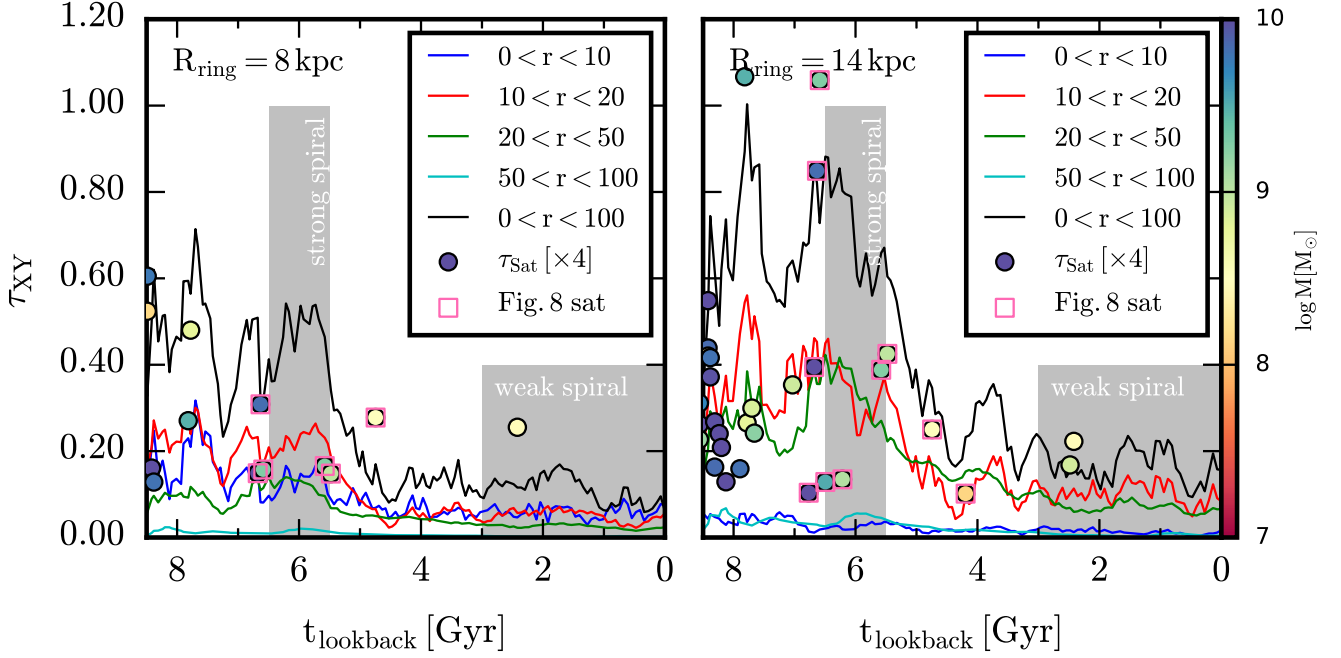


Figure 7. Evolution of the magnitude of the plane-parallel components of torque, τ_{XY} , exerted by dark matter particles on an 8 kpc (left) and 14 kpc (right) ring of evenly distributed test particles oriented along the disc plane (see text for details). The different coloured curves indicate the torque associated with spherical shells of dark matter particles, as indicated in the legend. The circles show the torque exerted by satellite galaxies (multiplied by a factor of 4 to aid visual comparison) and are coloured according to their total mass. For clarity, only points with $\tau_{XY} > 0.1$ are shown. The pink squares highlight the torque from a particular satellite (see Fig. 8 and text for details). Note the green point at $t_{\text{lookback}} \sim 6.5$ with $\tau_{XY} \sim 1$ (right-hand panel) and $\tau_{XY} \sim 0.18$ (left-hand panel) when the satellite was $\sim 5 \times 10^9 M_{\odot}$, which occurs of the order of 100 Myr prior to the peak torque from the dark matter halo inside 50 kpc: the latter torque is about 8 times larger than that of the former for $R_{\text{ring}} = 8$ kpc; and a factor of about 4 larger for $R_{\text{ring}} = 14$ kpc. The torque on each ring is dominated by the dark matter halo inside 50 kpc at all times. To guide the eye, grey shaded regions mark approximately the time periods when the phase spiral is particularly strong and weak (see Fig. 5), which correlate with the amplitude of the dark matter torque.

disc greater than that of the satellite behind which it formed. To show that a dark matter wake forms, we calculate an all-sky map of the dark matter overdensity in a spherical shell between galactocentric radii of 12 and 16 kpc by performing the following steps (see Gómez et al. 2016, for a more thorough description):

- (i) We apply a smoothing kernel to the dark matter particle distribution to estimate the density for each particle.
- (ii) We transform dark matter particle coordinates into spherical polar coordinates centred on the potential minimum of the galaxy, and for each particle in the spherical shell, calculate a polar grid of densities.
- (iii) We calculate an average density for the spherical shell to find the normalized dark matter overdensity at each grid point:

$$\hat{\rho} = \frac{\rho_{\text{grid}}(R, \phi, \theta) - \bar{\rho}_{\text{shell}}}{\bar{\rho}_{\text{shell}}}. \quad (5)$$

- (iv) To eliminate the triaxial halo signal from the map, we rotate the map by π in ϕ and flip along the $\theta = 0$ axis to produce $\hat{\rho}_{\text{flip}}(R, \phi, \theta)$, then calculate dipolar wake overdensity as

$$\delta\rho = \frac{\hat{\rho} - \hat{\rho}_{\text{flip}}}{2}. \quad (6)$$

To better visualize the all-sky map, we perform the procedure above on a re-simulation of the original halo Au 6 with a factor 8 higher dark matter mass resolution (see Appendix B for more details). The all-sky map for $\delta\rho$ at the time the dark matter-imparted torque reaches a maximum is shown in the upper panel of Fig. 9. The clear dipole observed is the signature of the wake, the major

axis of which is misaligned with the $\theta = 0$ vector that defines the mid-plane of the galactic disc. As shown by Gómez et al. (2017), a dark matter wake with a similar such alignment creates gravitational forces that act vertically on the disc to deform it into a warp-like pattern. The lower panel of Fig. 9 shows the all-sky map for $\delta\rho$ at $z = 0$: the wake has clearly decayed and all that remains is a relatively weak (and somewhat patchy) overdensity. This correlates with the sustained low and roughly constant torque at values ~ 5 times lower than the peak wake activity seen in the last few Gyr of evolution in Fig. 7, but still dominates over satellite-induced torque at all times. The phase spiral is left to wind up and decay during this late epoch into the comparatively weak pattern seen in Fig. 1.

4 CONCLUSIONS AND DISCUSSION

The *Gaia* phase spiral (Antoja et al. 2018), in addition to several other dynamical features (e.g. planar radial motions; Kawata et al. 2018), observed in the Milky Way is a sign that our Galaxy is in dynamical disequilibrium. The nature of the perturbation that set it in motion is the subject of much debate. Most of the theoretical work on the phase spiral has involved either very simplified toy models (Binney & Schönrich 2018) or idealized N -body simulations. Such numerical experiments sacrifice complex physics and cosmological environment for high resolution and/or a high degree of control over the set-up, and have provided several possible mechanisms including a buckling bar (Khoperskov et al. 2019) and the recent passages of Sgr (Laporte et al. 2019; Hunt et al. 2021).

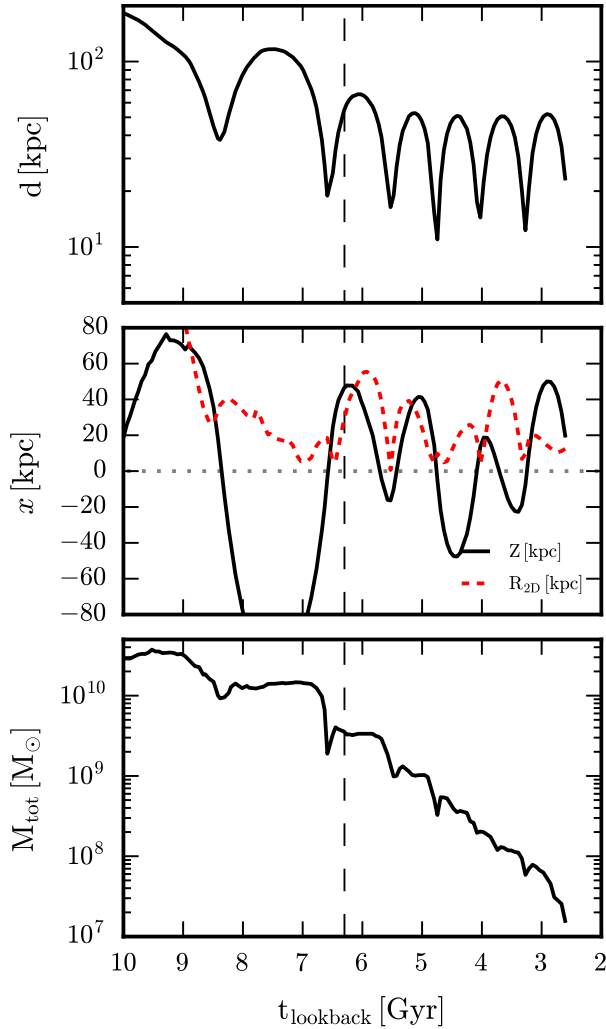


Figure 8. The evolution of the distance (top panel), vertical height and cylindrical radius (middle panel), and total mass (bottom panel) of the satellite responsible for generating the dark matter wake. The vertical dashed line indicates the time at which dark matter-induced torque reaches its peak (see Fig. 7).

In this paper, we have studied one of the first SUPERSTARS cosmological magnetohydrodynamical simulations containing $\sim 10^8$ disc star particles at $z = 0$. This provides a complementary view of the problem by connecting it to a wide range of dynamical phenomena inherent to galaxy formation in the Λ CDM cosmological paradigm, such as continued gas accretion and star formation, satellite interactions, and feedback. Our main conclusions are as follows:

(i) At late times ($t_{\text{lookback}} \lesssim 3$ Gyr) including the present day, our simulation shows a range of phase spiral features at multiple radii and azimuths over the stellar disc. At solar-like positions, phase spirals have typical overdensity amplitudes between ~ 0.05 and 0.15 and radial velocity amplitudes of $\sim 10 \text{ km s}^{-1}$. Remarkably, these properties are not unlike those of the *Gaia* snail shell despite all the complexities of the simulation and its differences with respect to the Milky Way. Our simulated phase spirals have 2–3 wraps in dimensionless coordinates – similar to the observed dimensionless phase spiral of Hunt et al. (2022) – but are more extended than observed in Z – V_Z coordinates.

(ii) The phase spirals are most clearly visible for coeval stellar populations of intermediate age (2–6 Gyr old), whereas older stars have a comparatively weak signal.

(iii) For star particles located in the outer disc ($R \sim 14$ kpc), phase spirals exhibit the same trends with age as for the solar-like populations, but are ‘squashed’ along the V_Z -axis owing to the lower disc surface density and vertical restoring force (in agreement with Laporte et al. 2019; García-Conde et al. 2022). They are also less tightly wound than their solar-position counterparts owing to their longer dynamical time-scales, which indicates that the outer Galactic disc is a promising place to look for signatures of past perturbations.

(iv) We present new insights into a scenario for the formation of the phase spiral: first, a satellite of total infall mass $\sim 10^{10} M_\odot$ generates the formation of a wake overdensity in the dark matter halo (see also Gómez et al. 2016) during its first pericentric passage $t_{\text{lookback}} \sim 6$ –7 Gyr. This dark matter wake generates a strong gravitational torque parallel to the disc; it is approximately eight times as strong as the direct torque imparted by the satellite at solar radii. As a result, a strong warp forms in the disc, which evolves into a global corrugation pattern. Locally, the oscillations associated with the corrugation pattern wrap up into spirals in the vertical phase plane.

(v) In our simulation, phase spirals are ever-present: they first appear during the early epochs of disc formation/evolution under the action of the dark matter halo wake, and are sustained until redshift zero, long after the main peak of the wake decays. The precise mechanism of this survival is unclear. However, idealized simulations have shown that the self-gravity of discs can maintain generations of bending waves for significant periods of time (e.g. Chequers & Widrow 2017; Chequers, Widrow & Darling 2018). We speculate that this mechanism occurs in our cosmological simulation as well, and defer a dedicated investigation to a separate future study.

Our findings have significance for the Sgr interpretation of the phase spiral: by fortuitous circumstance, the wake-inducing satellite shares many similar properties to the inferred orbit and mass-loss history of some dynamical models of Sgr (e.g. Vasiliev & Belokurov 2020). The main difference is that, in our simulation, its orbit is offset several gigayears into the past with respect to the real Sgr. A crude accounting of this offset would correspond to a ‘present-day’ satellite mass of $\sim 3 \times 10^8 M_\odot$, and a phase spiral like the one shown in the lower right-hand panel of Fig. 4, which would also be visible in the youngest stellar populations, in better qualitative accord with the age trends of observations (e.g. Bland-Hawthorn et al. 2019; Laporte et al. 2019). Thus, it seems plausible that a dark matter wake associated with the initial passages of Sgr could be playing a major role in the formation and propagation of the *Gaia* snail shell. This contrasts somewhat with the findings of recent idealized N -body simulations: for example, Laporte et al. (2018, 2019) showed that their Sgr analogue created a dark matter wake that dominated the torque on its first pericentric passage, but then subsequently decayed to a negligible level before direct torques from Sgr ‘reset’ the phase spiral pattern. It is possible that the properties of Milky Way-mass haloes and their satellite distributions in Λ CDM cosmological simulations alter the halo response of wake amplification processes (Vesperini & Weinberg 2000; Gómez et al. 2016) relative to idealized set-ups comprising a single object on a prescribed orbit in a smooth, spherical halo.

Importantly, a non-negligible role of a dark matter wake in the formation of the phase spiral could complicate the mapping between the phase spiral properties and those of Sgr. Indeed, the $\sim 10^{10} M_\odot$ infall mass of our wake-inducing satellite is somewhat less massive than that favoured by some idealized models (Laporte et al. 2019;

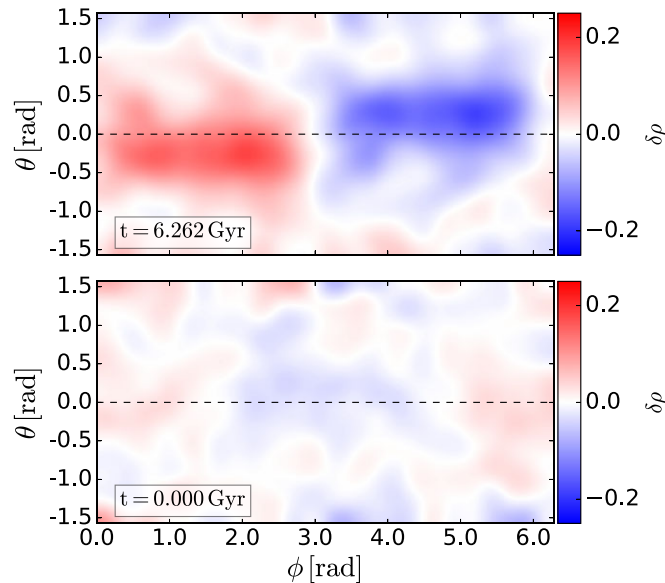


Figure 9. Overdensity maps, $\delta\rho$, obtained from the dark matter particles contained within a shell defined by spheres of 12 and 16 kpc galactocentric distances. These maps are obtained after rotating the original density by π in ϕ and flipping about $\theta = 0$, then subtracting this processed density map from the original in order to remove the quadrupolar triaxial halo feature. This enhances the dipolar signature of the wake, which is prominent at the time of maximum dark matter torque on the disc (upper panel) and inclined with respect to the disc mid-plane along $\theta = 0$ (dashed line). At the present day (lower panel), only a faint, patchy overdensity map remains.

Bland-Hawthorn & Tepper-García 2021), but may help alleviate some of the discrepancies between the mass of the Sgr remnant and phase spiral properties discussed by Bennett et al. (2022).

In addition to the mechanisms discussed in this paper, Tremaine et al. (2023) used a simple model to suggest that a separate collective response of many ‘Gaussian noise’ perturbations from subhaloes and/or giant molecular clouds can reproduce many properties of the phase spiral. While some of these types of perturbations should exist in our simulation, it is difficult to assess their prevalence and impact on the formation and destruction of the phase spiral alongside the other effects present. Controlled numerical simulations with prescribed spectra of small-scale perturbations would help clarify the situation.

With respect to other cosmological simulations, García-Conde et al. (2022) found that pericentric passages of a satellite of infall mass similar to that of our Sgr-like satellite correlated with the emergence of phase spirals in their simulation. However, they remark that the pericentre of this satellite is larger than that of Sgr and conclude that it is unlikely to be the sole contributor to the perturbation responsible for their phase spirals. We speculate that the dark matter halo wake mechanism discussed in this work is present also in their simulation.

Finally, we remark that the dynamical response of the disc to perturbations has a dependency on the kinematics of newborn coeval stellar populations, which in turn depends on our galaxy formation model as well as the precise assembly history of the simulated galaxy. For example, it is possible that the phase space coordinates of star particles older than ~ 6 Gyr just prior to the wake perturbation are different (perhaps dynamically hotter) than those of the Milky Way, which may explain the lack of clear signal for these star particles in our simulation. We note also that our simulation does not appear to produce the recently discovered two-armed phase spiral in the inner disc (Hunt et al. 2022); however, this may not be surprising because its origin is speculatively linked to bar/spiral structure, whereas our simulation does not contain a bar according to typical

definitions (e.g. Athanassoula 2002; Algorry et al. 2017; Fragkoudi et al. 2020). Thus, many questions remain open. Nevertheless, our results underline the difficulty in interpreting the complex dynamical history of the Galaxy, and expose a new link between phase spiral features like the *Gaia* snail shell and the dark matter distribution around the Galaxy. To make further progress on the phase spiral, future cosmological simulations with calibrated Sgr analogues will need to be performed. More generally, our study highlights the potential for a suite of SUPERSTARS simulations (Fragkoudi et al., in preparation) to scrutinize galactic dynamics in the cosmological context, such as the nature of galactic spiral arms and bar formation and evolution. We defer these tasks to future work.

ACKNOWLEDGEMENTS

The authors thank the referee for a prompt, constructive report. RJG acknowledges financial support from the Spanish Ministry of Science and Innovation (MICINN) through the Spanish State Research Agency, under the Severo Ochoa Program 2020–2023 (CEX2019-000920-S), and support from an STFC Ernest Rutherford Fellowship (ST/W003643/1). FAG acknowledges support from ANID FONDECYT Regular 1211370, the Max Planck Society through a ‘Partner Group’ grant, and ANID Basal Project FB210003. FvdV was supported by a Royal Society University Research Fellowship (URF\R1\191703). The authors gratefully acknowledge the Gauss Centre for Supercomputing e.V. (www.gauss-centre.eu) for funding this project by providing computing time on the GCS Supercomputer SUPERMUC-NG at Leibniz Supercomputing Centre (www.lrz.de).

DATA AVAILABILITY

High-level data underlying this article will be shared on reasonable request to the corresponding author.

REFERENCES

- Algorry D. G. et al., 2017, *MNRAS*, 469, 1054
- Antoja T. et al., 2018, *Nature*, 561, 360
- Antoja T., Ramos P., García-Conde B., Bernet M., Laporte C. F. P., Katz D., 2023, *A&A*, 673, A115
- Applebaum E., Brooks A. M., Christensen C. R., Munshi F., Quinn T. R., Shen S., Tremmel M., 2021, *ApJ*, 906, 96
- Athanassoula E., 2002, *ApJ*, 569, L83
- Bennett M., Bovy J., Hunt J. A. S., 2022, *ApJ*, 927, 131
- Binney J., Schönrich R., 2018, *MNRAS*, 481, 1501
- Binney J., Tremaine S., 2008, *Galactic Dynamics* 2nd edn. Princeton Univ. Press, Princeton, NJ
- Bland-Hawthorn J., Gerhard O., 2016, *ARA&A*, 54, 529
- Bland-Hawthorn J., Tepper-García T., 2021, *MNRAS*, 504, 3168
- Bland-Hawthorn J. et al., 2019, *MNRAS*, 486, 1167
- Briggs F. H., 1990, *ApJ*, 352, 15
- Chequers M. H., Widrow L. M., 2017, *MNRAS*, 472, 2751
- Chequers M. H., Widrow L. M., Darling K., 2018, *MNRAS*, 480, 4244
- Darling K., Widrow L. M., 2019, *MNRAS*, 484, 1050
- Faure C., Siebert A., Famaey B., 2014, *MNRAS*, 440, 2564
- Fragkoudi F. et al., 2019, *MNRAS*, 488, 3324
- Fragkoudi F. et al., 2020, *MNRAS*, 494, 5936
- Fragkoudi F., Grand R. J. J., Pakmor R., Springel V., White S. D. M., Marinacci F., Gómez F. A., Navarro J. F., 2021, *A&A*, 650, L16
- Frankel N., Bovy J., Tremaine S., Hogg D. W., 2023, *MNRAS*, 521, 5917
- Gaia Collaboration, 2018a, *A&A*, 616, A1
- Gaia Collaboration, 2018b, *A&A*, 616, A11
- Garavito-Camargo N., Besla G., Laporte C. F. P., Johnston K. V., Gómez F. A., Watkins L. L., 2019, *ApJ*, 884, 51
- García-Conde B., Roca-Fàbrega S., Antoja T., Ramos P., Valenzuela O., 2022, *MNRAS*, 510, 154
- Gargiulo I. D. et al., 2019, *MNRAS*, 489, 5742
- Genel S. et al., 2019, *ApJ*, 871, 21
- Gómez F. A. et al., 2012, *MNRAS*, 423, 3727
- Gómez F. A., Minchev I., O'Shea B. W., Beers T. C., Bullock J. S., Purcell C. W., 2013, *MNRAS*, 429, 159
- Gómez F. A., White S. D. M., Marinacci F., Slater C. T., Grand R. J. J., Springel V., Pakmor R., 2016, *MNRAS*, 456, 2779
- Gómez F. A., White S. D. M., Grand R. J. J., Marinacci F., Springel V., Pakmor R., 2017, *MNRAS*, 465, 3446
- Gómez F. A. et al., 2021, *ApJ*, 908, 27
- Grand R. J. J., Springel V., Gómez F. A., Marinacci F., Pakmor R., Campbell D. J. R., Jenkins A., 2016, *MNRAS*, 459, 199
- Grand R. J. J. et al., 2017, *MNRAS*, 467, 179
- Grand R. J. J. et al., 2018, *MNRAS*, 481, 1726
- Grand R. J. J. et al., 2021, *MNRAS*, 507, 4953
- Hunt J. A. S., Stelea I. A., Johnston K. V., Gandhi S. S., Laporte C. F. P., Bédorf J., 2021, *MNRAS*, 508, 1459
- Hunt J. A. S., Price-Whelan A. M., Johnston K. V., Darragh-Ford E., 2022, *MNRAS*, 516, L7
- Kawata D., Baba J., Ciucă I., Cropper M., Grand R. J. J., Hunt J. A. S., Seabroke G., 2018, *MNRAS*, 479, L108
- Khoperskov S., Di Matteo P., Gerhard O., Katz D., Haywood M., Combes F., Berczik P., Gómez A., 2019, *A&A*, 622, L6
- Laporte C. F. P., Johnston K. V., Gómez F. A., Garavito-Camargo N., Besla G., 2018, *MNRAS*, 481, 286
- Laporte C. F. P., Minchev I., Johnston K. V., Gómez F. A., 2019, *MNRAS*, 485, 3134
- Laporte C. F. P., Koposov S. E., Belokurov V., 2022, *MNRAS*, 510, L13
- Ludlow A. D., Schaye J., Schaller M., Richings J., 2019, *MNRAS*, 488, L123
- Ludlow A. D., Fall S. M., Schaye J., Obreschkow D., 2021, *MNRAS*, 508, 5114
- Marinacci F., Pakmor R., Springel V., 2014, *MNRAS*, 437, 1750
- Marinacci F., Grand R. J. J., Pakmor R., Springel V., Gómez F. A., Frenk C. S., White S. D. M., 2017, *MNRAS*, 466, 3859
- Monachesi A. et al., 2019, *MNRAS*, 485, 2589
- Monari G., Famaey B., Siebert A., Grand R. J. J., Kawata D., Boily C., 2016, *MNRAS*, 461, 3835
- Pakmor R., Marinacci F., Springel V., 2014, *ApJ*, 783, L20
- Pakmor R., Springel V., Bauer A., Mocz P., Munoz D. J., Ohlmann S. T., Schaaf K., Zhu C., 2016, *MNRAS*, 455, 1134
- Pakmor R. et al., 2017, *MNRAS*, 469, 3185
- Pakmor R., Guillet T., Pfrommer C., Gómez F. A., Grand R. J. J., Marinacci F., Simpson C. M., Springel V., 2018, *MNRAS*, 481, 4410
- Planck Collaboration XVI, 2014, *A&A*, 571, A16
- Poggio E. et al., 2018, *MNRAS*, 481, L21
- Purcell C. W., Bullock J. S., Tollerud E. J., Rocha M., Chakrabarti S., 2011, *Nature*, 477, 301
- Ruiz-Lara T., Gallart C., Bernard E. J., Cassisi S., 2020, *Nat. Astron.*, 4, 965
- Sanders J. L., Das P., 2018, *MNRAS*, 481, 4093
- Scannapieco C., White S. D. M., Springel V., Tissera P. B., 2009, *MNRAS*, 396, 696
- Schönrich R., Dehnen W., 2018, *MNRAS*, 478, 3809
- Shen J., Sellwood J. A., 2006, *MNRAS*, 370, 2
- Simpson C. M., Grand R. J. J., Gómez F. A., Marinacci F., Pakmor R., Springel V., Campbell D. J. R., Frenk C. S., 2018, *MNRAS*, 478, 548
- Slater C. T. et al., 2014, *ApJ*, 791, 9
- Springel V., 2010, *MNRAS*, 401, 791
- Springel V., Hernquist L., 2003, *MNRAS*, 339, 289
- Tian H.-J., Liu C., Wu Y., Xiang M.-S., Zhang Y., 2018, *ApJ*, 865, L19
- Tremaine S., Frankel N., Bovy J., 2023, *MNRAS*, 521, 114
- Trick W. H., Coronado J., Rix H.-W., 2019, *MNRAS*, 484, 3291
- Trick W. H., Fragkoudi F., Hunt J. A. S., Mackereth J. T., White S. D. M., 2021, *MNRAS*, 500, 2645
- Vasiliev E., Belokurov V., 2020, *MNRAS*, 497, 4162
- Vesperini E., Weinberg M. D., 2000, *ApJ*, 534, 598
- Vogelsberger M., Genel S., Sijacki D., Torrey P., Springel V., Hernquist L., 2013, *MNRAS*, 436, 3031
- Weinberg M. D., 1995, *ApJ*, 455, L31
- Weinberg M. D., 1998, *MNRAS*, 299, 499
- Widrow L. M., Gardner S., Yanny B., Dodelson S., Chen H.-Y., 2012, *ApJ*, 750, L41
- Widrow L. M., Barber J., Chequers M. H., Cheng E., 2014, *MNRAS*, 440, 1971
- Xu Y., Newberg H. J., Carlin J. L., Liu C., Deng L., Li J., Schönrich R., Yanny B., 2015, *ApJ*, 801, 105

APPENDIX A: PHASE SPIRALS AT THE PRESENT DAY

In this appendix, we present several versions of the phase spirals depicted in Fig. 1 in order to demonstrate how they depend on numerical resolution and the sample volume. We also show the dimensional counterpart for completeness.

Fig. A1 shows a version of Fig. 1 for the level 4 resolution simulation of the same halo. It is evident that phase spirals are not resolved at the present day at this resolution. This demonstrates the ability of our SUPERSTARS simulations to capture otherwise unresolved galactic dynamical structures.

Fig. A2 shows the phase spirals without normalizing Z and V_z by h_z and σ_z , respectively. In terms of both overdensity and radial velocity, the amplitudes of each phase spiral are essentially identical to the dimensionless phase spirals of Fig. 1. The phase spirals seem to extend to larger heights and velocities compared to the *Gaia* snail shell (e.g. Laporte et al. 2019; Antoja et al. 2023). The reason for this difference is unclear given that our simulation is not tailored to the Milky Way. We note also that our sample volume is larger than those typically probed by *Gaia*. Unfortunately, although the phase spirals for star particles selected from spheres of 1.5 kpc radius are discernible (see Fig. A3), they are evidently noisier and less clear than

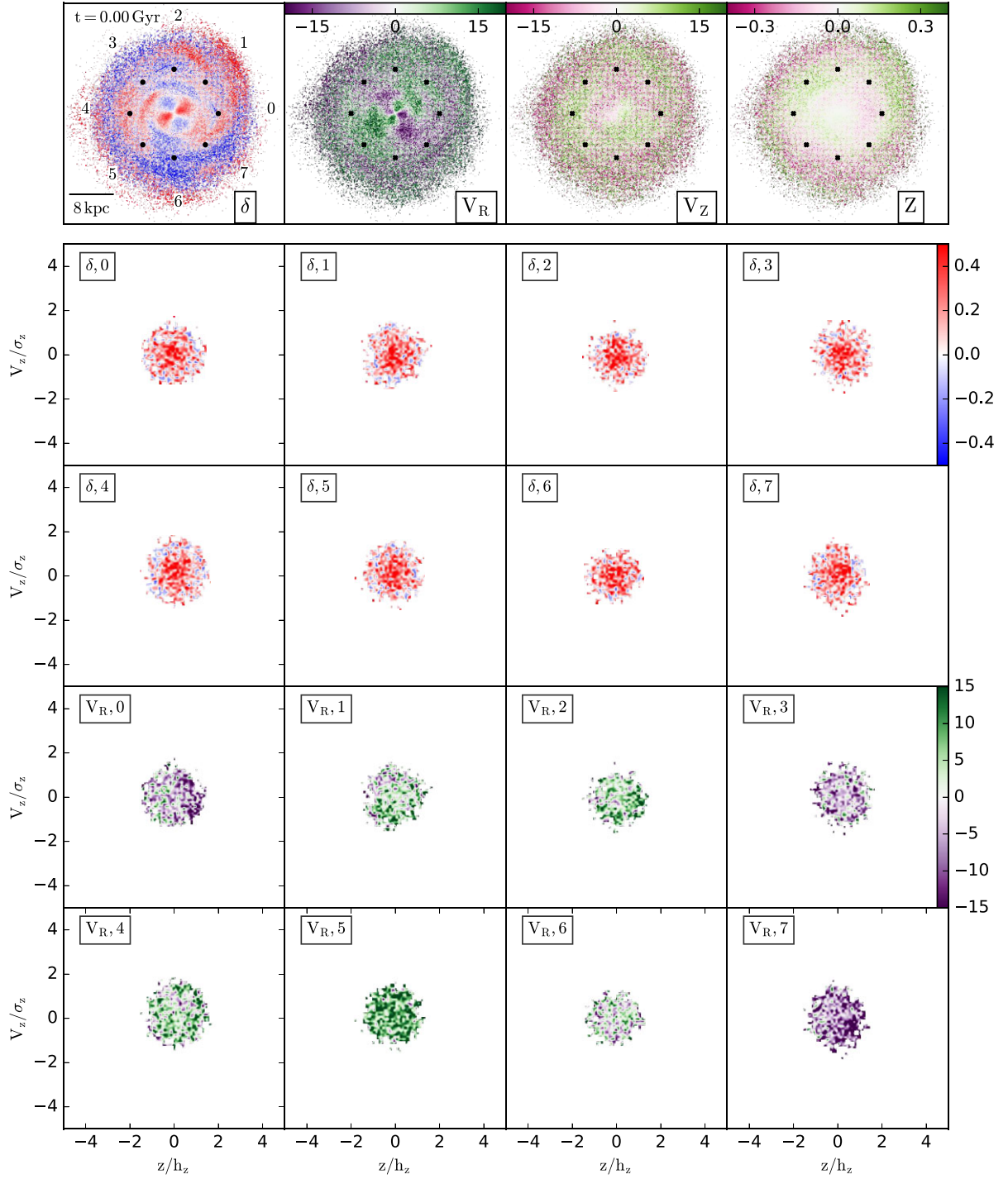


Figure A1. As Fig. 1, but for a simulation of the same halo at level 4 resolution: star particle mass of $\sim 5 \times 10^4 M_\odot$.

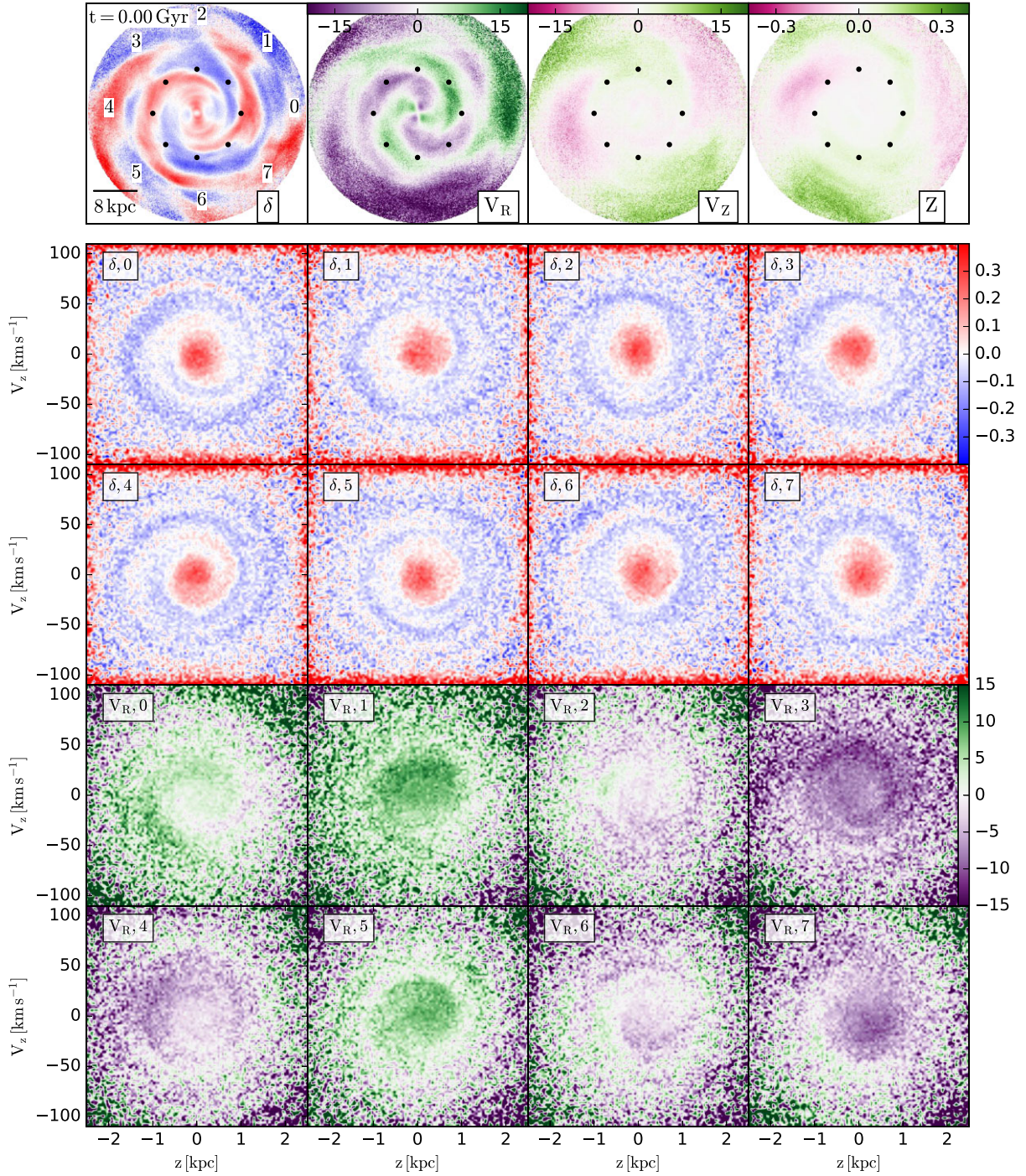


Figure A2. As Fig. 1, but the phase spirals are shown in the dimensional Z - V_Z plane. The amplitudes of both the overdensity (second and third rows) and the radial velocity (fourth and fifth rows) are the same as the dimensionless phase spirals shown in Fig. 1.

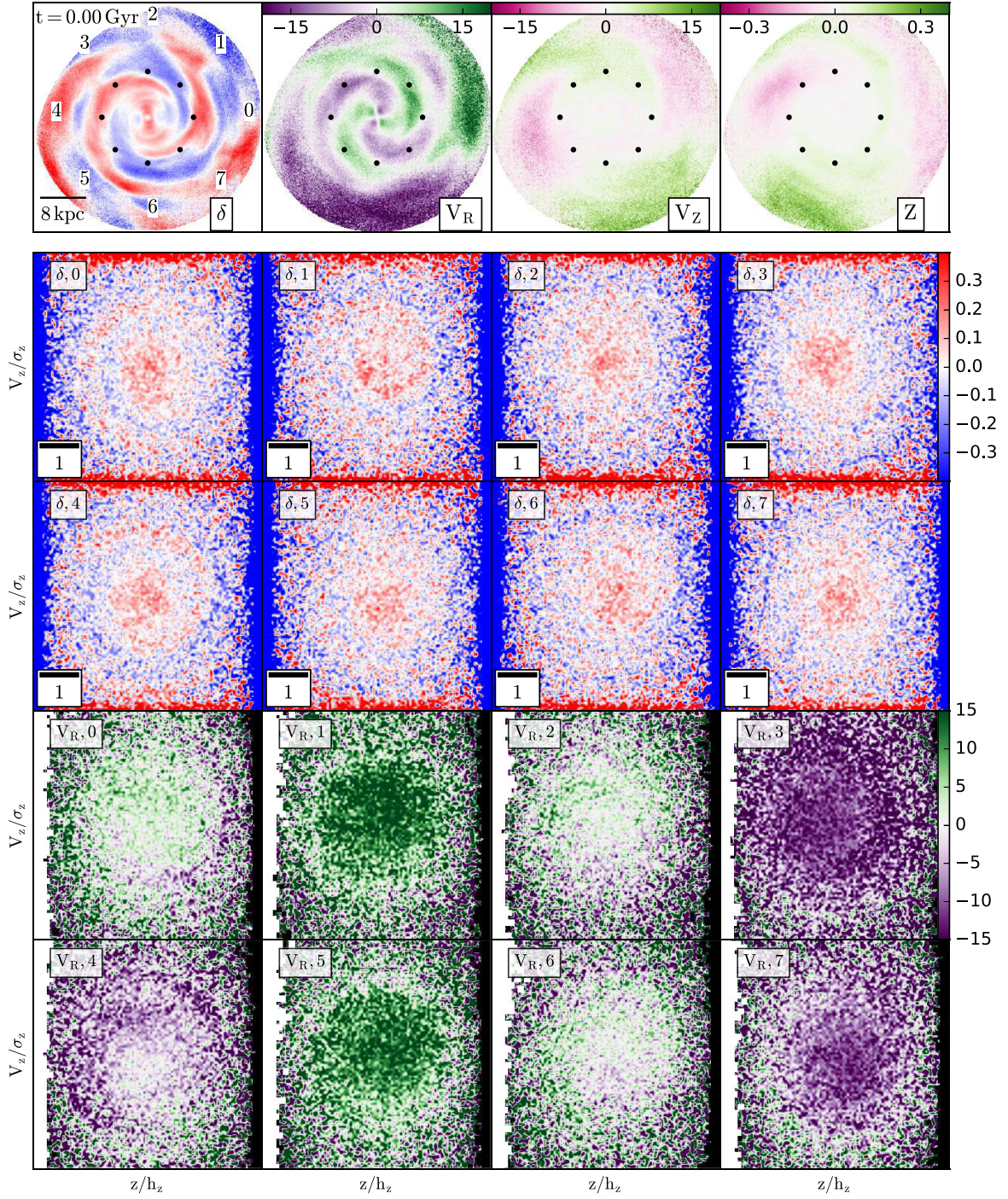


Figure A3. As Fig. 1, but for star particles selected in spheres of 1.5 kpc radii at solar-like positions. The range of the dimensionless axes have been shortened to ± 3 .

the 3 kpc volume shown in Fig. 1. We therefore opt to show the phase spirals clearly for 3 kpc spherical volumes throughout this paper.

APPENDIX B: RESOLUTION DEPENDENCE OF THE DARK MATTER WAKE

Because dark matter wakes develop over large volumes in the halo, it is logical to ask whether the dark matter particle resolution is high enough (and noise low enough) to capture the dynamics (e.g. Garavito-Camargo et al. 2019). To demonstrate that the torques induced by the dark matter wake are robust to resolution changes, Fig. B1 shows a reproduction of the right-hand panel of Fig. 9 for the SUPERSTARS simulation (here denoted by ‘SUPERSTARS64’) as well as a re-simulation of the same system, ‘DM8’ with eight times as many dark matter particles (but with the standard single star particle formed per gas cell, i.e. ‘level 4’ stellar resolution). It is evident that, for each radial shell considered, the salient features of the evolution of the torque acting perpendicular to the disc minor axis are preserved at both resolution levels. The main appreciable difference is that the strength of the torque decays more slowly after the peak at ~ 6 Gyr for the DM8 run compared to the SUPERSTARS64 run. However, the difference is slight and could potentially be accounted for by minor stochastic variations in, for example, the precise infall time, mass, and orbit of the wake-generating satellite; such variations can arise from the ‘butterfly effect’ phenomenon (e.g. Genel et al. 2019; Grand et al. 2021) or resolution changes (although we note that the evolution of the putative satellite in the SUPERSTARS64 and DM8 simulations is almost identical). Nevertheless, the convergence seen in Fig. B1 indicates that the torque imparted by the dark matter wake is captured in our SUPERSTARS simulation.

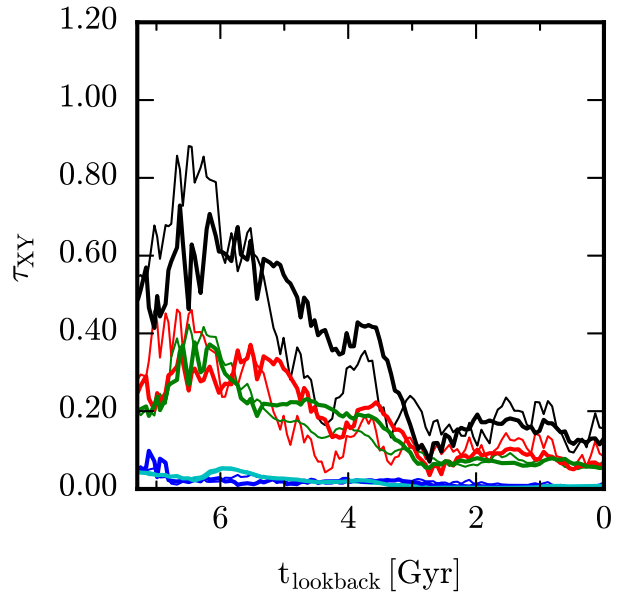


Figure B1. As the right-hand panel of Fig. 7, but for the dark matter torques from a re-simulation with eight times better dark matter resolution (denoted by DM8; thick curves) as well as the fiducial simulation (denoted by SUPERSTARS64; thin curves). Each thin curve traces its thick curve counterpart very well, which indicates a high level of convergence for dark matter-induced torque.

This paper has been typeset from a \LaTeX file prepared by the author.